

Microstructure and mechanical characteristics of bulk polycrystalline Ni consolidated from blends of powders with different particle size

G. Dirras^{a,*}, J. Gubicza^b, S. Ramtani^a, Q.H. Bui^a, T. Szilágyi^b

^a LPMTM-CNRS, UPR 9001, Université Paris 13, 99 Avenue J.B. Clément, 93430 Villetaneuse, France

^b Department of Materials Physics, Eötvös Loránd University, Budapest, P.O.B. 32, H-1518, Hungary

ARTICLE INFO

Article history:

Received 3 June 2009

Received in revised form

24 September 2009

Accepted 25 September 2009

Keywords:

Nickel

Powder metallurgy

Multi-modal microstructure

Mechanical properties

ABSTRACT

Near fully dense polycrystalline nickel with a random crystallographic texture was consolidated by hot isostatic pressing of blends of nanocrystalline and conventional microcrystalline powders with different volume fractions. The transformation process resulted in a composite-like microstructure constituted by clusters of soft coarse grains regularly distributed in a hard ultrafine-grained matrix. It was found that the ultrafine-grained matrix hinders the coalescence of the coarse grains component during sintering resulting in a smaller grain size than in the fully coarse-grained counterpart in a sort of “barrier effect”. This effect was found to depend on the volume fraction of the ultrafine-grained matrix. Conversely, during the hot isostatic pressing, the plastic deformation of the coarse-grained fraction is preferred to that of the ultrafine-grained fraction, because of greater dislocation activity in the former type of grains, resulting in lower defect densities in the ultrafine-grained matrix (“shielding effect”). It is shown that as a result of the interplay between the coarse-grained and ultrafine-grained components during sintering, the mechanical behavior of the composite materials cannot be obtained by a linear interpolation between the characteristics of fully ultrafine-grained and coarse-grained counterparts.

© 2009 Elsevier B.V. All rights reserved.

1. Introduction

The improvement of the physical–chemical and mechanical properties of materials is generally obtained by different ways of microstructure modification such as grain size reduction, development of multi-modal grain size distribution, and tailoring grain-boundary structure. Among the several ways to process bulk materials with such microstructures, the compaction of powders has a fundamental place because of its versatility to tailor *in-demand* composite-like microstructures. This type of process allows obtaining centimeter-scale and fully dense materials having different grain sizes spanning the nanometer (30–100 nm) range to the ultrafine-grained, UFG (100–1000 nm) regime and above [1,2].

On the one hand, nanocrystalline materials (NC) have so far demonstrated interesting physical–chemical properties and improved mechanical characteristics. Nevertheless, while higher flow stress or fracture stress, in comparison to their coarse-grained (CG) counterparts have been demonstrated in a number of studies [3–5], other properties such as ductility, which is a key parameter in forming processes still need to be improved. Indeed, the lack of sufficient ductility and toughness has slowed down the potential application of these materials in structural components. The

low ductility has been attributed to the limited dislocation storage capability and dislocation mobility of NC materials, which results in the absence of work hardening leading to plastic instability.

On the other hand, different strategies have been proposed to offset the low tensile ductility accompanying the high flow stress of NC and UFG materials [6,7]. Focusing on pure face-centered cubic NC metals, it has been demonstrated that controlled volume fraction of twins in Cu induces both high strength and considerable tensile ductility, the latter being due to the strain rate sensitivity improvement by the presence of coherent twin boundaries, TBs [8–11]. Another strategy for the improvement of ductility of NC and UFG materials is the incorporation of coarse grains in a fine-grained matrix as proposed in recent studies by Wang and Ma [6], Ahn et al. [12] and Newbery et al. [13]. In this case, the improvement of ductility can be attributed to the larger dislocation activity of coarse grains (storage and mobility) thereby enhancing the strain hardening capability of materials. The bimodal grain-structure can be achieved by heterogeneous grain-growth in severely deformed materials such as Cu [14], Al–0.6Zr [15] or Ni [16] or by abnormal grain-growth caused by microstructure heterogeneities such as inhomogeneous solute distribution and/or residual porosity [17]. In a recent work [16], bimodal and multi-modal grain size distributions have been generated in bulk Ni by combining cryomilling and hot consolidation. These samples yielded ductility of 42% and 49% for the bulk multi-modal and bimodal samples respectively, compared to a ductility of about 48% for the CG sample. The yield

* Corresponding author. Tel.: +33 1 49 40 34 88.

E-mail address: dirras@univ-paris13.fr (G. Dirras).

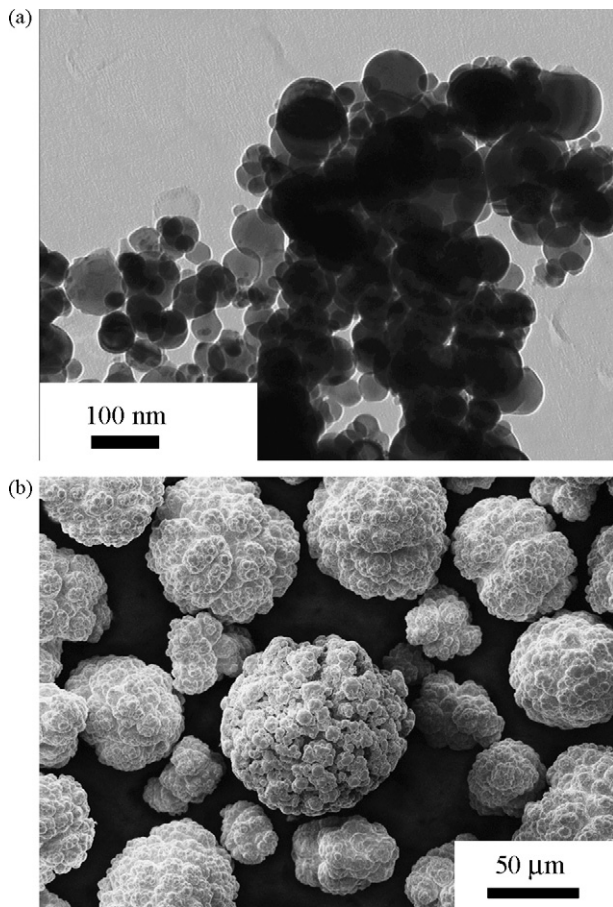


Fig. 1. The microstructure of the starting Ni powders. (a) TEM image of NP powder with an average particle size of 100 nm; (b) SEM picture showing clusters in CP powder with an individual particle size of about 5 μm .

strengths of multi-modal, bimodal and CG samples were about 457 MPa, 312 MPa and 157 MPa, respectively. Beside the heterogeneous grain-growth in severely deformed materials, another way to produce bimodal grain structures is the sintering of blends of CG and NP powders which is scarcely studied in the literature [18,19].

In this paper, the effect of addition of a well-controlled volume fraction of CG powder to a harder UFG Ni matrix on the microstructure of the consolidated materials and their mechanical properties are studied. The relationship between the microstructure and the mechanical behavior, and the underlying mechanisms of plastic deformation at room temperature (RT) are investigated.

2. Experimental procedures

2.1. Material processing

Bulk samples were processed from blends of high purity ($\sim 99.9\%$) Ni nanopowder (NP) with a conventional coarse-grained powder (CP). The NP powder was supplied by Argonide Corporation (Sanford, FL) and was synthesized by electro-explosion of wires [20]. The transmission electron microscopy (TEM) image in Fig. 1a shows that the NP powder consists of spherically shaped particles

Table 2

The optimized parameters for the HIP cycle processing for the different powder compositions.

	HIP conditions		
	T_p [$^{\circ}\text{C}$]	P [MPa]	t [min]
UFG	700	140	150
CG	700	160	150
Sample A	700	156	155
Sample B	640	145	60

T_p , P and t are the temperature, pressure and duration of HIP, respectively.

having an average size of about 100 nm. The particles in the CP powder (produced by Goodfellow) were agglomerated into particle clusters of about 50 μm in diameter as it is revealed by the scanning electron microscopy (SEM) image in Fig. 1b. The average size of the individual particles within the clusters was about 5 μm . The chemical composition of the initial powders determined by Inductively Coupled Plasma Spectroscopy (ICP/OES) is given in Table 1.

Along with bulk samples processed from 100% NP and 100% CP powders (hereafter referred to as UFG and CG samples, respectively), two additional specimens with different volume fractions of NP and CP powders were prepared. Sample A was processed by mixing ~ 33 vol.% CP and ~ 67 vol.% NP powders while for sample B the relative amount of the CP powder was only ~ 17 vol.%. The powders including the blends were handled and prepared in a glove box under inert gas (Ar) flow to minimize possible contamination. To reach an optimum distribution of the CP particles within the NP powder, the powders were mixed in a three-dimensional shaker mixer (Turbula[®] model T2F) for 6 h at RT. The different powders/blends were filled into stainless steel cans and degassed at room temperature for 1 week before consolidation using hot isostatic pressing (HIP).

The HIP procedure has been described in our previous papers [1,2,21]. The processing conditions were optimized to reach the desired microstructure having small porosity. The pressure, the temperature and the duration of the HIP cycles were set around 150 MPa, 700 $^{\circ}\text{C}$ and 150 min, respectively, with slight variation from sample to sample due to their different powder compositions, as it can be seen in Table 2. The pressure and the temperature were applied concomitantly. Both the heating and cooling rates were equal to 375 K/h.

The microstructure characteristics of the consolidated samples were investigated by electron backscattering diffraction (EBSD) and scanning electron microscopy (SEM). Both EBSD and SEM analyses were conducted by a conventional LEO S360 microscope. The EBSD scans covered regions of approximately 350 $\mu\text{m} \times 350 \mu\text{m}$ using a step size between neighboring measurement positions of 0.1 μm . Post-data treatment was carried out using the software OIM version 4 from TexSEM Laboratories (TSL).

To complement EBSD and SEM investigations, the microstructure of the consolidated samples was further investigated by X-ray line profile analysis. The X-ray line profiles were measured by a high-resolution rotating anode diffractometer (Nonius, FR591) using $\text{CuK}\alpha_1$ radiation. The scattered X-rays were detected by imaging plates with an angular resolution of 0.005 $^{\circ}$ in 2θ , where θ is the angle of diffraction. The line profiles were evaluated using the extended Convolutional Multiple Whole Profile (eCMWP) fitting procedure described in detail in other reports [22,23]. In this

Table 1

Chemical composition of the initial NP and CP powders in ppm.

	Ni	Ca	Cu	Fe	Mg	Mn	S
NP powder	Base	824 \pm 15	485 \pm 10	434 \pm 8	926 \pm 10	93 \pm 3	<10
CP powder	Base	115 \pm 3	93 \pm 3	20.9 \pm 0.5	199 \pm 3	32 \pm 2	<6

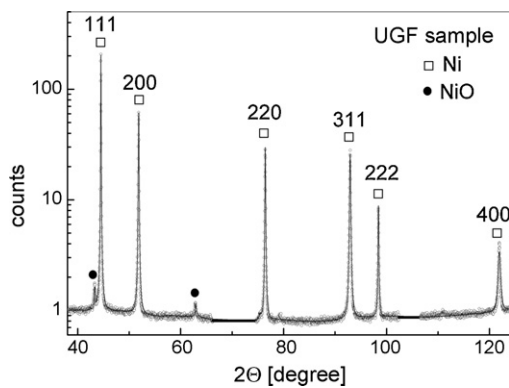


Fig. 2. The measured (open circles) and the fitted (solid line) X-ray diffraction patterns for the UFG sample in logarithmic intensity scale.

method, the experimental pattern is fitted by the convolution of the instrumental pattern and the theoretical size and strain line profiles. The theoretical profile functions used in this fitting procedure are calculated on the basis of a model of the microstructure, where the crystallites have spherical shape and log-normal size distribution, and the lattice strains are assumed to be caused by dislocations and twins. This method gives the dislocation density and the twin fault probability with good statistics. The twin fault probability is defined as the fraction of the faulted $\{111\}$ planes (these are the TBs) along their normal vector.

The mechanical properties were studied by quasi-static compression and nanoindentation tests at RT. The compression tests were carried out on prismatic specimens with the dimensions of $3\text{ mm} \times 3\text{ mm} \times 5\text{ mm}$ using an Instron universal testing machine (model 1195) at a strain rate of $1.6 \times 10^{-4}\text{ s}^{-1}$. The strain was calculated from the crosshead displacement corrected by the stiffness of the machine. The local mechanical behavior of the four samples was studied by nanohardness measurements using an UMIS nanoindentation device with Berkovich indenter tip and applying a maximum load of 2 mN. The indentation rate was 0.15 mN s^{-1} . 400 indentations were carried out arranging the indents in a 20×20 matrix. The distance between the neighboring indents was $20\text{ }\mu\text{m}$. The maximum indentation depth was between 100 and 250 nm depending on the actual hardness value, which corresponds to the indent size between $0.7\text{ }\mu\text{m}$ and $1.7\text{ }\mu\text{m}$. The hardness is calculated as [24]

$$H = \frac{P_m}{24.5h_m^2} \quad (1)$$

where P_m is the maximum load (2 mN) and h_m is the maximum penetration depth during indentation.

3. Results and discussion

3.1. Microstructure of the consolidated Ni samples

After HIP-processing, the density of each compact has been determined using Archimedes' principle [1]. The relative densities were 96%, 98%, 97% and 94% for the UFG and CG specimens, and samples A and B, respectively. It is observed that the CG sample yielded the highest density among the four samples, and the higher the fraction of NP powder in the blends, the lower the relative density of the consolidated samples. This is partially due to the fact that despite the care taken during powder handling, the surface of the powders oxidized resulted in NiO oxide content in the consolidated samples as revealed by XRD investigations (see Fig. 2). In the XRD experiments, the oxide content was determined as the integrated intensity ratio of NiO and Ni peaks at $2\theta = 43.3^\circ$ and 44.5° , respec-

tively, in the diffraction patterns. It should be noted that this ratio does not give the NiO phase content in the samples and it is only used for the comparison between the samples investigated here. The intensity ratios are 0.29%, 0.45% and 0.6% for sample A, sample B and the UFG materials, respectively. No significant amount of NiO phase was detected for the CG sample. It can be seen that the higher the NP powder content in the blend, the higher the NiO content in the consolidated specimen. Consequently, the lower density of NiO (6.67 g/cm^3) compared to Ni (8.902 g/cm^3) contributes to the decrease of relative density of the samples with increasing UFG content. It should also be noted that the lowest density for sample B is most probably caused by incomplete particle bonding and residual porosity due to the relatively low temperature and short duration of HIP.

3.1.1. Grain structure from SEM and EBSD

Fig. 3 shows SEM images of the microstructure for samples A and B and for the CG specimen. The following observations can be made:

- (i) As expected from HIP-processing [1,2], the microstructures obtained here exhibit a random crystallographic texture. As an example, the colored EBSD insert in Fig. 3b illustrates the random orientation distribution of the grains of the CG cluster in the drawn square shape. EBSD investigations also showed that in both samples A and B, the majority of the boundaries (92% and 95% for samples A and B, respectively) are high angle grain boundaries.
- (ii) The fractions of the CG and UFG components are 61% and 39% for sample A, respectively, while these values are 39% and 61% for sample B. For both samples, the CG fraction evaluated from SEM data is higher than the volume fraction of the CP component in the powder blends measured before consolidation (see Section 2.1). This difference can be explained by the more dense powder microstructure in the CP powder compared to NP powder component. The dense particle packing in the CP powder is supported by the agglomeration of the particles in Fig. 1.
- (iii) The CG clusters were homogeneously distributed within the UFG matrix. The average size of the CG clusters was the same (about $50\text{ }\mu\text{m}$) in samples A and B than in the initial CP powder, i.e., the CP agglomerate-size remained unchanged during consolidation of the blended specimens.
- (iv) At the same time, the mean grain size inside the CG clusters increases with decreasing UFG fraction, and their values are $13\text{ }\mu\text{m}$ and $7\text{ }\mu\text{m}$ for samples A and B, respectively. In the consolidated CG sample, the grain size ($50\text{--}100\text{ }\mu\text{m}$) is close or even higher than the agglomerate size in the initial CG powder. This indicates a grain-coalescence inside the CG agglomerates during HIP, which may also spread into the neighboring agglomerates. In the composite samples it seems that the UFG component acts against the coalescence of CG grains as the higher the UFG content, the lower the level of grain-growth in the CG component. Most probably, during powder mixing, NP particles got in between CG agglomerates which formed thin intergranular UFG domains between CG grains in the consolidated samples. The higher oxide content in this UFG component hinders the grain-boundary motion of CG grains during sintering, hereby lowering the grain-coalescence. This can be called as a "barrier effect" of UFG fraction on CG grains. Nevertheless, the lower degree of grain-coalescence in CG component of sample B can be partially attributed to the lower temperature and shorter time of sintering. It is noted that thermodynamic consideration suggests that coarser grains should grow at the expense of UFG grains during sintering of powder blends due to the higher specific grain-boundary area of the smaller grains. Consequently, if the UFG fraction had been oxide-free, its addition to the CG

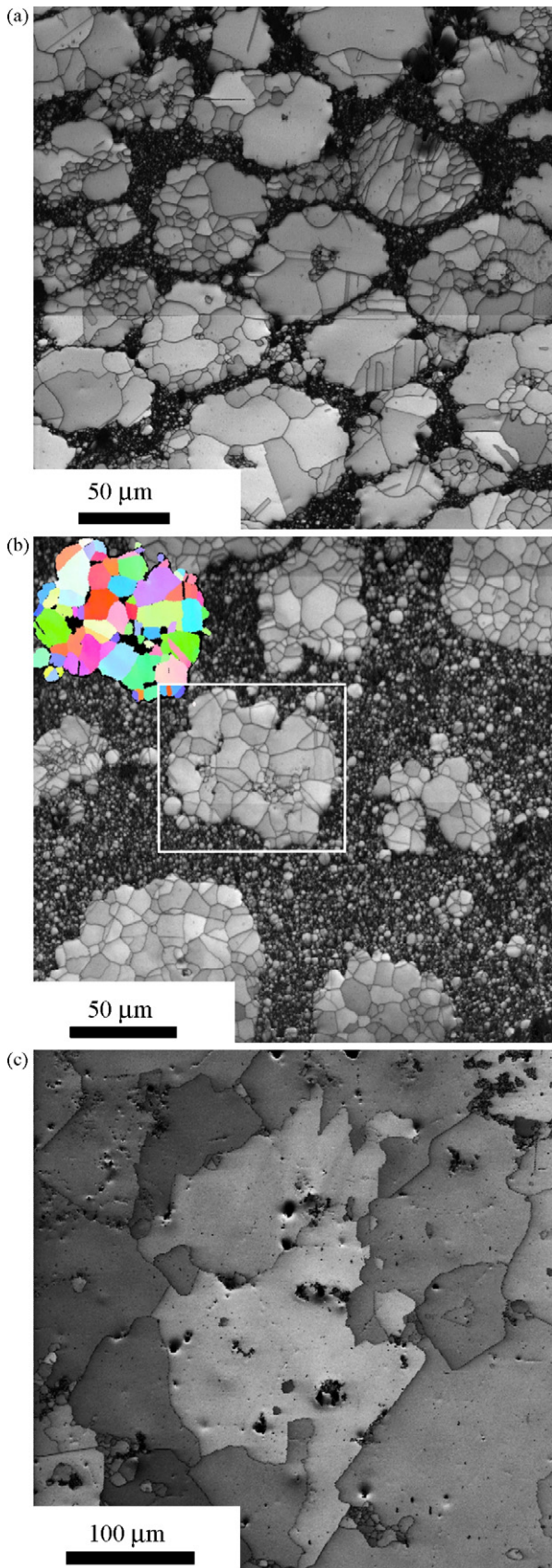


Fig. 3. SEM images of the microstructure for the composite samples A (a) and B (b). For comparison, picture for the CG specimen is also shown (c). As an example, the colored EBSD insert in (b) illustrates the random orientation distribution of the grains in a CG component (enclosed in the square shape).

component most probably would have accelerated the grain coarsening during sintering.

- (v) TEM experiments (not shown here) indicate that the UFG grains have a log-normal size distribution with an average grain size of about 400 nm in the fully UFG specimen and also in samples A and B.

In the following, for the sake of clarity, the composite microstructures will be considered simply as being bimodal microstructures constituted by a UFG component with an average grain size lower than 1 μm and a CG component with an average grain size larger than 1 μm .

3.1.2. Microstructure by X-ray line profile analysis

To complement EBSD and SEM investigations, the microstructure of the initial samples was studied by X-ray line profile analysis. As an example, the fitting of the X-ray diffraction pattern for the UFG sample is shown in Fig. 2. The open circles and the solid line represent the measured data and the fitted curves, respectively. It should be noted that for samples A and B, sharp intensity spots were visible in the Debye–Scherrer rings which are related to the reflecting CG grains. These peaks of CG grains were as narrow as the instrumental profiles ($\Delta(2\theta) = 0.02^\circ$), therefore these lines were not evaluated for the microstructure. For the determination of the microstructural parameters of the UFG volume, the parts of the Debye–Scherrer rings free from sharp spots were cut and evaluated. The microstructural parameters of the CG sample were not determined by X-ray line profile analysis as its peaks were as narrow as the instrumental profiles.

The mean crystallite size, the dislocation density (ρ) and the twin fault probability (β) determined for the UFG fraction of the as-received samples A and B as well as for the UFG sample are listed in Table 3. The crystallite size (~ 200 nm) determined by X-ray line profile analysis is lower than the grain size observed by TEM for the UFG component of the as-received samples (~ 400 nm). This phenomenon has been usually observed for plastically deformed bulk metals [25] and it can be attributed to the fact that the crystallite size determined from X-ray line profiles corresponds essentially to the mean size of cells/subgrains which is usually smaller than the conventional grain size measured in metals by electron microscopy methods [26]. The plastic deformation during high temperature sintering most probably also results in the formation of subgrains which act as coherently scattering domains with average size less than the grain size measured by TEM.

Table 3 shows that after the HIP operation the dislocation density and the twin probability in the UFG volumes of samples A and B are much lower than in the UFG sample. This observation can be explained by a “shielding effect” of CG grains on the UFG fraction during consolidation. The “shielding effect” means that at the contact places between the NP and CP powder particles, the deformation of the softer CP particles is larger than in the NP particles when they fill the empty spaces in the composite materials during consolidation. Moreover, the NP particles in the pockets between CP clusters are most probably protected from external stresses. As a consequence of the moderate deformation of NP particles, the dislocation density and the twin probability are smaller in the UFG grains after HIP-processing. Despite the lower CG content of sample B, which should result in a weaker “shielding effect” on the UFG component, the dislocation density and the twin probability of the latter are not higher than the values characteristic for sample A. This may be attributed to the shorter sintering time in the case of sample B.

Table 3The crystallite size, the dislocation density (ρ) and the twin fault probability (β) obtained by X-ray line profile analysis.

Sample	Crystallite size [nm]	ρ [10^{14} m^{-2}]	β [%]
Sample A, as-received, UFG fraction	219 \pm 20	0.7 \pm 0.2	0.00 \pm 0.05
Sample A, $\varepsilon = 0.12$, whole sample	185 \pm 15	4.8 \pm 0.5	0.00 \pm 0.05
Sample A, $\varepsilon = 0.30$, whole sample	106 \pm 11	6.2 \pm 0.7	0.10 \pm 0.05
Sample B, as-received, UFG fraction	139 \pm 15	0.3 \pm 0.2	0.00 \pm 0.05
Sample B, $\varepsilon = 0.12$, whole sample	149 \pm 15	6.7 \pm 0.7	0.00 \pm 0.05
Sample B, $\varepsilon = 0.30$, whole sample	76 \pm 8	6.8 \pm 0.7	0.10 \pm 0.05
UFG, as-received, whole sample	139 \pm 15	5.6 \pm 0.5	0.32 \pm 0.05
UFG, $\varepsilon = 0.35$, whole sample	49 \pm 5	16 \pm 2	0.00 \pm 0.05

3.2. Mechanical behavior of the consolidated samples

3.2.1. Compression tests

Fig. 4a shows the resulting true stress–true plastic strain curves for samples A and B, along with the data obtained for the fully UFG and CG specimens. The yield strength was plotted as a function of the UFG volume fraction in Fig. 4b. It can be seen that the yield strength increases with increasing the amount of the UFG content of the samples. For example, the yield strength of sample B (~ 270 MPa) is about 26% higher than that of sample A (~ 200 MPa), but about half of the yield strength for the UFG counterpart (~ 510 MPa). Fig. 4b shows that the yield strength values determined for samples A and B can be found under the straight line connecting the data points of the fully CG and UFG samples. This means that the yield strength of the composite-like materials cannot be obtained by a linear interpolation from the strength values of the fully CG and UFG specimens. Most probably, this can be attributed to the fact that the microstructure in either the CG or

UFG components is strongly affected by the volume fraction of the other component (“barrier and shielding effects”).

The strain hardening rate (SHR) of the four samples evolves differently during compression tests (see Fig. 4a). In the early stage of plastic deformation (up to a plastic strain of about $\varepsilon = 0.01$) the SHR of sample B is higher than that of sample A. It is also observed that for plastic strains between 0.05 and 0.15, the SHR behaves similarly for samples A and B. Afterwards, the SHR of sample A decreases more rapidly than for sample B. At $\varepsilon \approx 0.3$, the SHR values for samples A and B are smaller than that for the fully UFG sample in spite of their larger CG fractions. This may be attributed to: (i) the weaker boundary strength due to the “shielding effect” in the UFG component and (ii) the crack-formation at the grain-boundaries as a result of elastic strain incompatibility between the UFG and CG components as discussed in Section 3.2.5. The fully UFG sample exhibits a steady-state-like regime from about $\varepsilon = 0.05$ to 0.25 with a SHR of ~ 1 GPa. At the same time, the flow stress of the fully CG sample increases progressively and the SHR values ($1 \text{ GPa} < \text{SHR} < 3 \text{ GPa}$) being larger in the whole deformation range compared to the other samples.

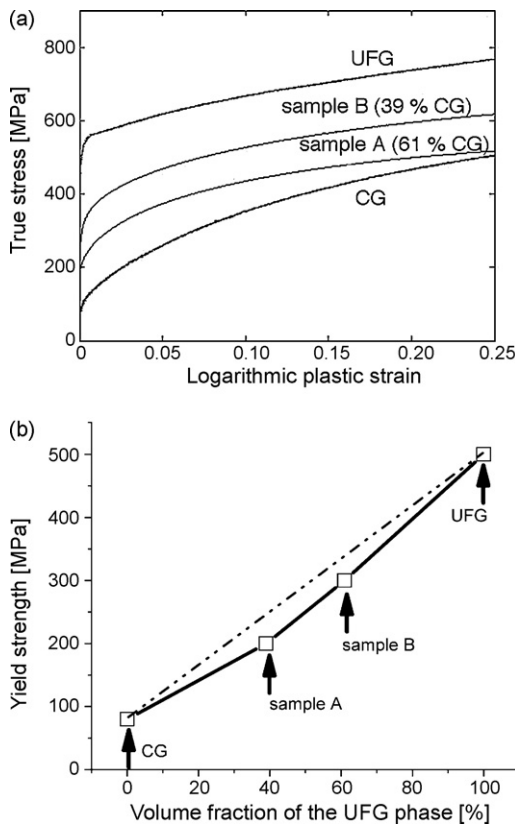


Fig. 4. (a) True stress–logarithmic plastic strain curves obtained by compression test at RT for the four consolidated samples. The volume fraction of the CG component is also indicated. (b) The yield strength values obtained from the stress–strain curves in (a).

3.2.2. Characterization of the hardness of the CG and UFG components by nanoindentation

The strength of the CG and UFG components was characterized locally by nanoindentation. The nanohardness distributions for the fully CG specimen, samples A and B, and for the fully UFG specimen are shown in Fig. 5. The mean hardness increases in the following order: CG specimen (2.4 ± 0.1 GPa), sample A (3.3 ± 0.1 GPa), sample B (4.9 ± 0.1 GPa) and UFG specimen (7.1 ± 0.1 GPa). It can be seen that the mean nanohardness increases with increasing the UFG content of the samples which is in line with the trend observed for the yield strength. At the same time, the hardness for samples A and B is smaller than the values interpolated from the hardness values characteristic for the fully CG and UFG specimens. This observation is in line with the results obtained for yield strength.

It can be seen from Fig. 5 that the hardness distributions for samples A and B are asymmetric having long tail in the higher hardness region. This tail part is most probably related to the UFG component of the microstructure. The low-hardness part of the distribution is assumed to be related to the CG component. The mean hardness of the CG component was determined by averaging the lowest hardness values up to the 61% and 39% of the total number of indentations for samples A and B, respectively (these are the relative fractions of the CG components). The mean hardness of the UFG component was estimated by averaging 39% and 61% of hardness numbers having the highest values for samples A and B, respectively.

The hardness values of the CG and UFG components for different samples are plotted in Fig. 6. The hardness of the fully CG sample is lower than that for the CG fraction in sample A which is lower than the hardness of the CG component in sample B. This can be explained by the decrease of the grain size in the CG component with increasing UFG volume fraction (“barrier effect”). It should be noted that the relative number of indents located in the CG grains

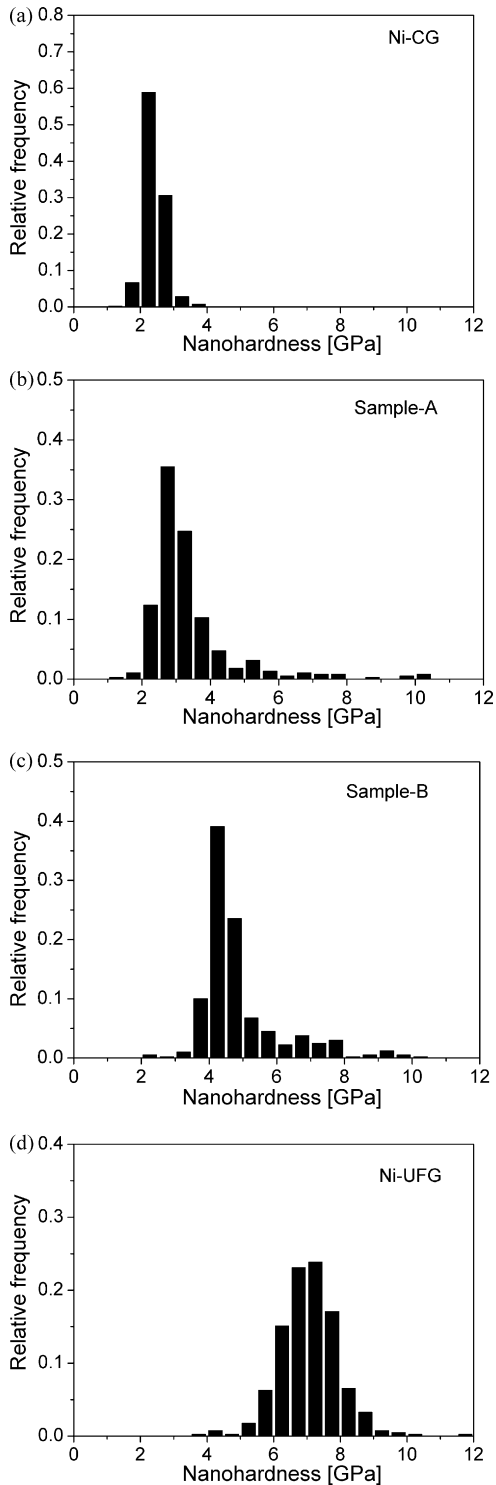


Fig. 5. The nanohardness distributions for (a) the CG specimen, (b) sample A, (c) sample B and (d) the UFG specimen.

may differ slightly from the volume fraction of the CG component which may result in slight deviation of the calculated mean hardness from the real value. It should be also noted, that some hardness values measured in the CG grains may be affected by the hardness of the UFG grains and *vice versa* as the size of an indent is determined by the strength of a volume around the indent having a radius of about 20 times the penetration depth. For example, close to the interfaces between the CG and UFG grains the hardness of the CG grains may be higher than in the center of the CG grains, or the

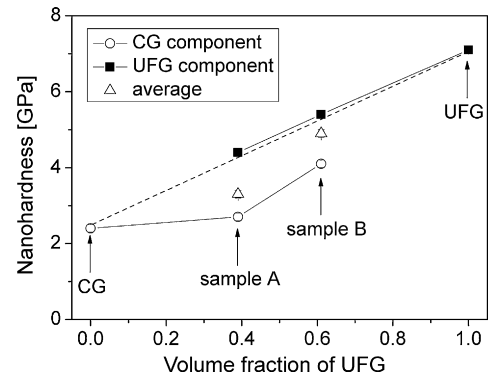


Fig. 6. The nanohardness of the CG and UFG fractions, and their volume-weighted average as a function of the volume fraction of the UFG component for the as-processed CG specimen, sample A, sample B and UFG specimen. The dashed line represents the linear interpolation between the values characteristic for the fully CG and UFG samples.

hardness of the UFG component may be lower if there is a CG grain under the measured UFG region.

Fig. 6 shows that in the composite samples the hardness of the UFG component is lower than that in the fully UFG sample, and it seems that the higher the CG fraction, the lower the hardness of the UFG component. This can be explained by the “shielding effect” of the CG grains on the UFG volumes during sintering as discussed in Section 3.1.2. As a result of this effect, the dislocation density is smaller in the UFG grains after HIP-processing resulting in lower hardness of the UFG component. The “shielding effect” of the CG component may also yield incomplete particle bonding within the UFG component which also contributes to the lower hardness. In the case of sample B, the lower hardness of the UFG component may be partially caused by the lower relative mass density which is most probably associated with a higher porosity due to the lower temperature and shorter duration of sintering. The smaller hardness of the UFG component in samples A and B compared to the

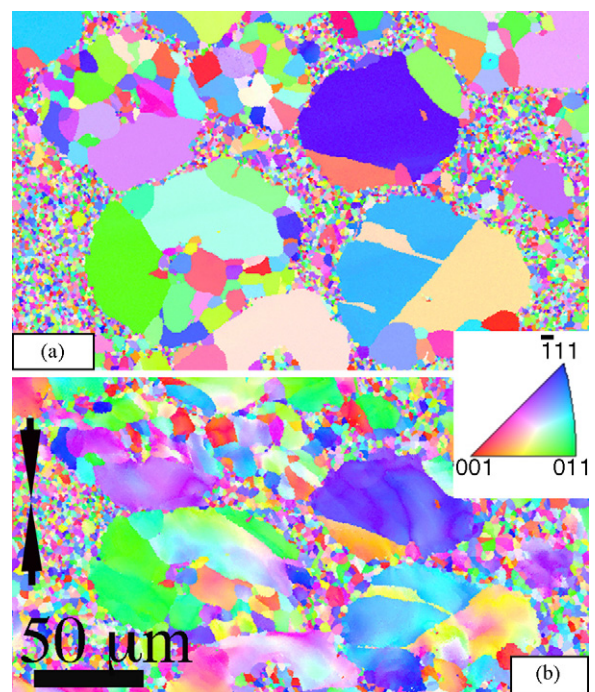


Fig. 7. EBSD images taken on the same lateral surface area of sample A: (a) before compression test and (b) after compression up to a strain of 12%. The black arrows in (b) indicate the direction of the compressive load.

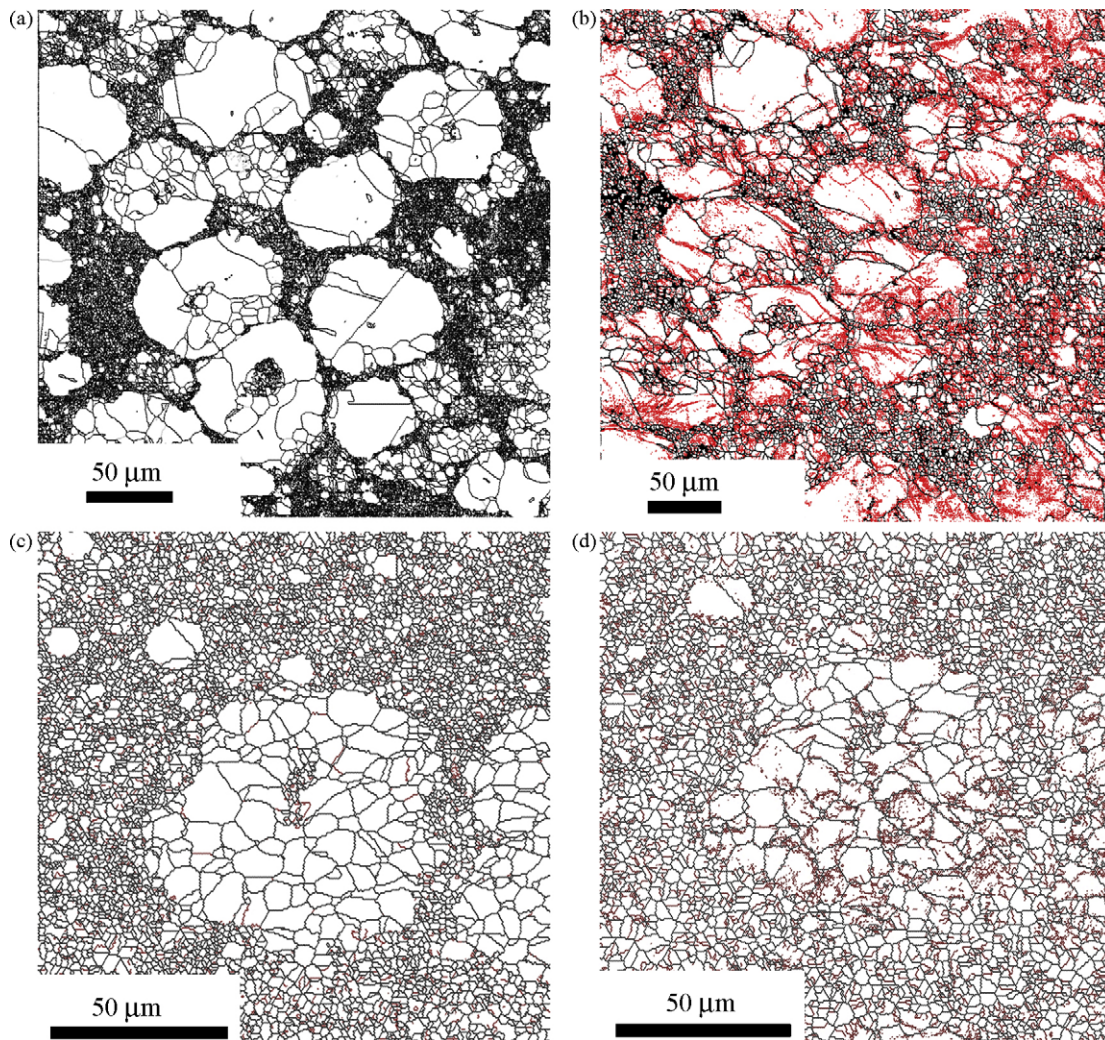


Fig. 8. EBSD boundary maps for sample A: (a) before compression, (b) after compression up to a strain of 12% and for sample B, (c) before compression, and (d) after compression up to a strain of 12%. The red and black lines represent the low angle grain boundaries having misorientation between 2° and 15° and the high angle grain boundaries with larger misorientations, respectively. (For interpretation of the references to color in this figure legend, the reader is referred to the web version of the article.)

fully UFG specimen is primarily responsible for the smaller hardness and yield strength of the composite samples than the values interpolated from the data characteristic for the fully CG and UFG samples (see Figs. 5 and 6).

3.2.3. EBSD investigation of the microstructure after compression

Fig. 7 illustrates the microstructure evolution in sample A during compression test by comparing the EBSD images taken on the same area before compression and after the sample has been deformed up to a plastic strain of about 12%. It can be seen that the misorientation inside the grains of the CG component increased during plastic straining as a result of dislocation activity and formation of subgrains.

Based on the morphology changes of CG grains in Fig. 7, the mean computed strain for these grains is about 29% which is about twice than the imposed macroscopic strain (12%) similarly as reported previously on coarse Al grains embedded in UFG Al matrix [1]. The larger strain of the CG grains may be a result of strain localization during compression. The strain may be localized in a cross-section of the sample where the area fraction of soft CG component is larger than the average.

Fig. 8 shows the changes in the grain-boundary structure during plastic deformation of the composite samples. In this figure, the red and black lines represent the low angle grain boundaries (LAGBs)

having misorientations between 2° and 15° and the high angle grain boundaries (HAGBs) with larger misorientations, respectively. In the initial non-deformed state (see Fig. 8a), the majority of the boundaries are HAGBs (92% including TBs). After deformation up to a strain of 12%, a tremendous increase of LAGBs is observed within the CG component most probably as a result of clustering of dislocations. The majority of LAGBs are formed in the vicinity of HAGBs (see Fig. 8b) as the latter boundaries act as obstacles to dislocations. A large fraction of LAGBs is also observed at the UFG/CG interfaces. At the same time, the twin boundary fraction decreased from about 11% to 3% which is a consequence of the interaction between TBs and dislocations, as reported in a previous work [21]. The formation of LAGBs and the decrease of the fraction of TBs indicate that the plastic deformation is basically controlled by dislocations at RT. It is noted that the zero twin probabilities determined by X-ray line profile analysis for the as-received samples A and B (see Table 3) are not in contradiction with the finite values of TB fraction obtained by EBSD as these values are under the detection limit of line profile analysis.

Fig. 8c and d shows the grain-boundary maps for sample B before compression and after deformation up to a strain value of 12%. Sample B shows the same behavior as sample A. It is clear from Fig. 8d that after compression the majority of LAGBs are located in the vicinity of the grain boundaries and twin boundaries. It is

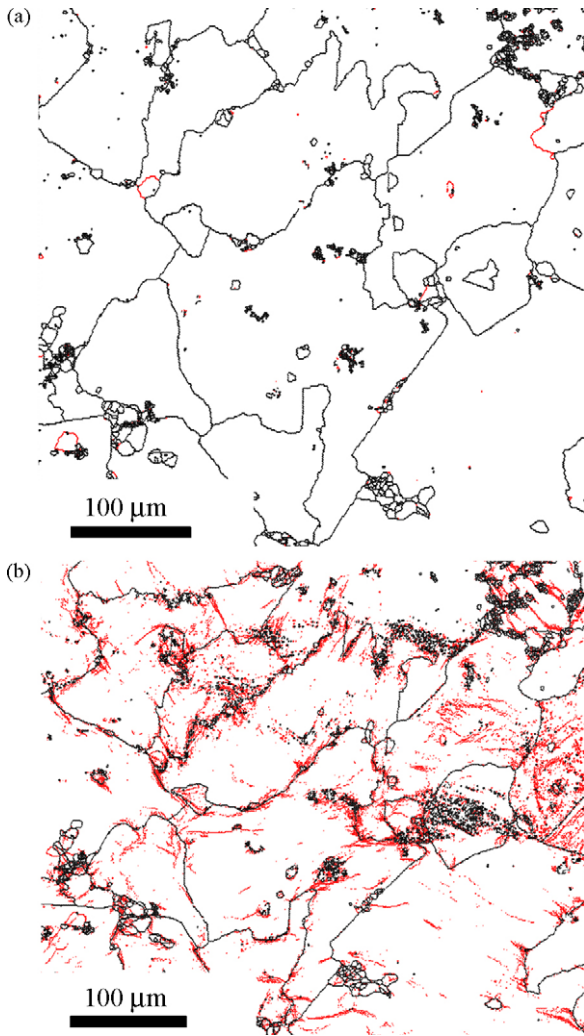


Fig. 9. EBSD boundary maps for the: (a) as-processed CG sample and (b) after compression up to a strain of 12%. The red and black lines represent the low angle grain boundaries having misorientation between 2° and 15° and the high angle grain boundaries with larger misorientations, respectively. (For interpretation of the references to color in this figure legend, the reader is referred to the web version of the article.)

noted that the change of the shape of the CG grain-clusters in sample B during compression appears to be smaller than for sample A (compare Figs. 7 and 8). This can be explained by a less localized deformation in sample B compared to sample A, which can be attributed to the lower hardness difference of the CG and UFG components in sample B. The ratios of the hardness values for the CG and UFG fractions are 1.6 and 1.3 for samples A and B, respectively (see Fig. 6). The lower hardness difference between the two components in sample B decreases the probability of occurrence of strong plastic flow localization. Fig. 9a and b shows the EBSD boundary maps for the consolidated CG sample before compression and after a strain of 12%. The increase of LAGBs within the grains and at GBs is evidenced. The formation of LAGBs is a consequence of an extensive dislocation activity and storage inside the grains enhancing the strain hardening capability as it is observed in the true strain–true stress compression curve for the CG sample (see Fig. 4a)

3.2.4. Microstructure evolution during compression test as determined by X-ray line profile analysis

The change of the parameters of the microstructure during compression test was also monitored by X-ray line profile analysis. The mean crystallite size, the dislocation density and the twin fault

probability were determined for samples A and B as well as for the UFG sample at strains of 12% and 30%, and listed in Table 3. As it was mentioned in Section 3.1.2, for the as-received samples A and B only the parts of the Debye–Scherrer rings free from the sharp intensity spots were evaluated, therefore the obtained microstructural parameters were characteristic only for the as-received UFG component. In the case of the deformed samples A and B, due to the grain refinement and the increase of the dislocation density in the CG component during deformation, the Debye–Scherrer rings were relatively homogeneous, therefore the scattered intensities from the UFG and CG fractions were not separated in the evaluation of the line profiles. This means that for these samples the microstructural parameters characterize the whole sample.

It can be seen that the dislocation density increases during compression which indicates that the plasticity in both CG and UFG components is mainly controlled by dislocations at RT. The mean dislocation density after deformation at $\varepsilon = 0.12$ is higher for sample B compared to sample A, which can be attributed to the higher UFG content. In the UFG component, the NiO content is most probably higher than in the CG component because the NP powder has larger oxidized surface area than the CP powder as discussed in Section 3.1. The higher NiO content results in higher rate of dislocation multiplication as suggested in Ref. [27]. The dislocation density is the highest for the UFG sample at $\varepsilon = 0.35$ which is in line with the highest NiO content and the largest dislocation density in the as-received UFG sample.

Table 3 shows that the crystallite size was reduced for all the three samples after compression up to $\varepsilon \approx 0.3$. The degree of the decrease of crystallite size in samples A and B is difficult to estimate as for the as-received samples the crystallite size could be determined only for the UFG components while after compression the crystallite size values are characteristic for the whole samples. The decrease of crystallite size most probably occurs by the clustering of dislocations into cell/subgrain boundaries [25,26]. The mean crystallite size at $\varepsilon \approx 0.3$ is smaller for sample B than for sample A which can be explained by the higher UFG fraction, the smaller crystallite size in the as-received UFG component and the smaller grain size in the as-received CG component in sample B compared to sample A, as indicated by the present EBSD and X-ray line profile experiments.

Table 3 shows that for samples A and B the twin probability remained at very low level during compression at RT. For the fully UFG specimen, the twin probability is reduced owing to “detwinning” caused by dislocations as reported in Ref. [21]. The decrease of the twin density during compression is in agreement with the present EBSD observations.

3.2.5. SEM analysis of the fracture surfaces

Fig. 10 shows the fracture surfaces observed in SEM investigation in the composite materials after the failure of the samples in compression test. Fig. 10a indicates two different modes of rupture: while the failure of the UFG component appears to be rather a brittle type, the CG component experienced large deformation before failure that occurred in a ductile manner as shown by the presence of micro-cavities (bottom of the CG component) and slip patterns (top right). Notice also the presence of cracks at the interface between the UFG matrix and the CG component.

Fig. 10b exemplified the fracture surface representative for sample B. Here the CG component is subdivided into smaller grains ($\sim 7 \mu\text{m}$). Beside cracks that can be clearly seen at the boundaries between the CG and UFG components, it is observed that each grain within the CG cluster has experienced plastic deformation and the slip lines inside the different grains have various orientations. The cracks at the interfaces of the CG and UFG components may be caused by elastic strain incompatibilities between the two components. The stresses needed for the same plastic deformation in the

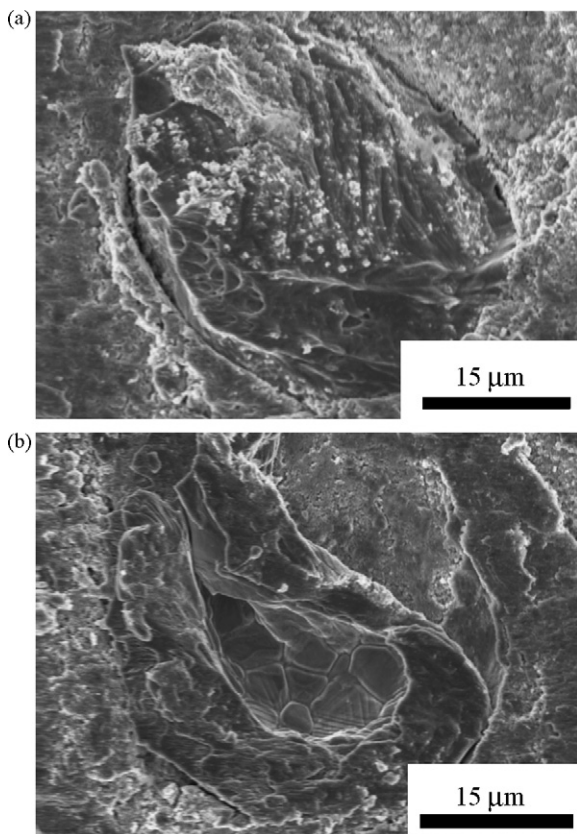


Fig. 10. SEM images showing the fracture surfaces of the composite materials: (a) sample A and (b) sample B.

two components are different as the CG component is softer than the UFG component. The different stresses probably cause various elastic strains in the CG and UFG fractions resulting in mismatch stresses at the interfaces which may facilitate the crack propagation at these boundaries. The strain incompatibilities between the CG grains having different slip directions may also yield easier failure of the sample, unless the grains accommodate the strain-difference by activating another mechanism, especially at the grain boundaries. The brittle fracture in the UFG fraction is most probably caused by the presence of oxides that embrittled the grain boundaries, leading to intergranular fracture [21]. The weak particle bonding due to the “shielding effect” of the CG component may also contribute to the fracture at the grain boundaries in the UFG fraction.

4. Conclusions

Near fully dense and crystallographic texture-free polycrystalline nickel samples have been consolidated by HIP from blends of nanocrystalline and conventional microcrystalline powders with different volume fractions. The sintered materials have composite-like microstructures with clusters of CG grains embedded in an UFG matrix. The CG and UFG components are formed from the CP and NP powder fractions, respectively. From the investigation of the microstructure and the mechanical behavior of the consolidated samples, the following conclusions have been drawn.

The UFG component hinders the grain-coalescence of the CG grains during high temperature sintering resulting in a smaller

grain size in the CG component with increasing UFG fraction. We called this phenomenon as a “barrier effect” of the UFG fraction on the CG component.

The CG crystals plastically deform in preference to the UFG grains during sintering thereby resulting in a lower dislocation density in the UFG component. We called this as a “shielding effect” of the CG grains on the UFG component.

It was found that the higher the amount of the UFG component, the higher the strength and hardness of the specimens. At the same time, the hardness of the composite samples cannot be obtained by a linear interpolation between the hardness values of the fully UFG and CG materials. This can be explained by the dependence of the hardness of the CG and UFG fractions on the amount of the other component due to the “barrier and shielding effects”.

The increase of the dislocation density and the LAGB fraction, the reduction of the crystallite size and the TB density indicate that the plastic deformation at RT is basically controlled by dislocations in these hot consolidated Ni samples, irrespectively of their grain size.

Acknowledgments

G. Dirras is very grateful for the support of the National Research Agency (ANR 09-BLAN-0010-01). The authors are obliged to Mrs. P. Szommer and J.-P. Michel for processing nanohardness measurements and HIPing operations respectively.

References

- [1] S. Billard, J.P. Fondere, B. Bacroix, G.F. Dirras, *Acta Mater.* 54 (2006) 411–421.
- [2] W.Q. Cao, G.F. Dirras, M. Benyoucef, B.J. Bacroix, *Mater. Sci. Eng. A* 462 (2007) 100–105.
- [3] G.E. Fougère, M. Ferber, J. Weertman, R.W. Siegel, *Mater. Sci. Eng. A* 204 (1995) 1–6.
- [4] R.W. Siegel, G.E. Fougere, *Nanostruct. Mater.* 6 (1995) 205–216.
- [5] C.C. Koch, D.G. Morris, K. Lu, A. Inoue, *Mater. Res. Soc. Bull.* 24 (1999) 54–58.
- [6] Y.M. Wang, E. Ma, *Acta Mater.* 52 (2004) 1699–1709.
- [7] A.A. Fedorov, M.Y. Gutkin, I.A. Ovid'ko, *Scripta Mater.* 47 (2002) 51–55.
- [8] M. Dao, L. Lu, R.J. Asaro, J.T.M. De Hosson, E.J. Ma, *Acta Mater.* 55 (2007) 4041–4065.
- [9] M. Dao, L. Lu, Y.F. Shen, S. Suresh, *Acta Mater.* 54 (2006) 5421–5432.
- [10] L. Lu, R. Schwaiger, Z. Shan, M. Dao, K. Lu, S. Suresh, *Acta Mater.* 33 (2005) 2169–2179.
- [11] R. Schwaiger, B. Moser, M. Dao, N. Chollacoop, S. Suresh, *Acta Mater.* 51 (2003) 5159–5172.
- [12] B. Ahn, E.J. Lavernia, S.R. Nutt, *J. Mater. Sci.* 43 (2008) 7403–7408.
- [13] A.P. Newbery, B. Ahn, P. Pao, S.R. Nutt, E.J. Lavernia, *Adv. Mater. Res.* 29–30 (2007) 21–29.
- [14] C. Lu, Y.W. Mai, Y.G. Shen, *J. Mater. Sci.* 41 (2006) 937–950.
- [15] V.L. Tellkamp, E.J.J. Lavernia, *Nanostruct. Mater.* 12 (1999), pp. 249–252.25.
- [16] Y.H. Zhao, T. Topping, J.F. Bingert, J.J. Thornton, A.M. Dangelewicz, Y. Li, W. Liu, Y.T. Zhu, Y.Z. Zhou, E.L. Lavernia, *Adv. Mater.* 20 (2008) 3028–3033.
- [17] V.Y. Gertsman, R. Birringer, *Scripta Metall. Mater.* 30 (1994) 577–581.
- [18] D. Witkin, Z. Lee, R. Rodriguez, S. Nutt, E. Lavernia, *Scripta Mater.* 49 (2003) 297–302.
- [19] Y. Wang, M. Chen, F. Zhou, E. Ma, *Nature* 419 (2002) 912–915.
- [20] Y.-S. Kwon, Y.-H. Jung, N.A. Yavorovsky, A.P. Illyin, J.-S.J. Kim, *Scripta Mater.* 44 (2001) 2247–2251.
- [21] J. Gubicza, H.Q. Bui, F. Fellah, G.F. Dirras, *J. Mater. Res.* 24 (2009) 217–226.
- [22] G. Ribarik, J. Gubicza, T. Ungar, *Mater. Sci. Eng. A* 387–389 (2004) 343–347.
- [23] L. Balogh, G. Ribarik, T. Ungar, *J. Appl. Phys.* 100 (2006) 023512.
- [24] F. Frohlich, P. Grau, W. Grellmann, *Phys. Stat. Sol. A-Appl. Res.* 42 (1977) 79–89.
- [25] Y.T. Zhu, J.Y. Huang, J. Gubicza, T. Ungar, Y.M. Wang, E. Ma, R.Z. Valiev, *J. Mater. Res.* 18 (2003) 1908–1917.
- [26] J. Gubicza, N.Q. Chinh, Z. Horita, T.G. Langdon, *Mater. Sci. Eng. A* 387–389 (2004) 55–59.
- [27] F.J. Humphreys, J.W. Martin, *Philos. Mag.* 16 (1968) 927–957.